Studying stearic acid interaction with ZnO/SiO$_2$ nanoparticles with tailored morphology and surface features: a benchmark for better designing efficient ZnO-based curing activators.

Silvia Mostoni [a], Paola Milana [a], Massimiliano D'Arienzo [a], Sandra Dirè [b], Emanuela Callone [b], Cinzia Cepek [c], Silvia Rubini [c], Aysha Farooq [c] Carmen Canevali [a], Barbara Di Credico [a] and Roberto Scotti [a]*

[a] Department of Materials Science, INSTM, University of Milano-Bicocca, Via R. Cozzi 55, 20125 Milano, Italy;

[b] Department of Industrial Engineering (DII), University of Trento, Via Sommarive 9, 38123, Trento, Italy;

[c] Istituto Officina dei Materiali-CNR Laboratorio TASC, Strada Statale 14, km 163.4, I-34012 Trieste, Italy

KEYWORDS: Zinc oxide; Vulcanization; Activator; Stearic acid; surface interaction.

18   ABSTRACT

19   The interaction between activators (ZnO) and co-activators (stearic acid, SA) represents a key step

20   in the vulcanization process, to generate Zn(II) intermediate complexes that enhance the reaction

21   kinetic and promote the shortening of sulfur bridges, leading to highly cross-linked materials. To

22   understand the influence of the structural, morphological and surface properties of ZnO in the

23   reactivity with SA, in this work, pure ZnO nanoparticles (NPs) and ZnO NPs anchored on SiO_2

24   (ZnO/SiO_2) were prepared through soft chemistry techniques. Tailoring of morphology and

25   surface features was accomplished through a fine control of the synthetic parameters, as

26   demonstrated by the careful characterization of the activators. Then, the interaction of pure ZnO

27   and ZnO/SiO_2 activators with SA in the absence of rubber was investigated by using Differential

28   Scanning Calorimetry (DSC). The occurrence of Zn(II)-SA complexes with different thermal

29   stability and structural properties was assessed by a comprehensive thermogravimetric and

30   spectroscopic survey. The generation and the chemical structure of these specific vulcanization

31   intermediates was related to the peculiar characteristics of the ZnO/SiO_2 systems and, in turn, to

32   their ability in imparting faster kinetics and higher curing efficiency to isoprene rubber

33   nanocomposites, compared to bare ZnO.

34   These results, besides proposing a valid benchmark for achieving further insights on the interaction

35   of stearic acid with activators, pave the way to provide specific protocols for a better design and

36   implementation of ZnO-based materials able to effectively enhance the rubber vulcanization

37   process, with significant economic and environmental advantages.

38

39

40   INTRODUCTION

41   The performances of rubber materials, used in different applications as tires, strongly depend on

42   the sulfur vulcanization process, as it enables the formation of sulfur-based chemical cross-links

43   between the elastomer chains that contribute to the reinforcement of the organic matrix [1-5]. To

44   facilitate the sulfur interaction with the elastomer, shorten the vulcanization time and lower the

45   energy consumption, curing agents are employed [1-11]. These are: i) organic accelerators such as

46   N-cyclohexyl-2-benzothiazole sulfenamide (CBS) and tetramethylthiuram disulfide (TMTD) [3],

47   ii) inorganic activators, like ZnO [6-10] and iii) co-activators as fatty acids (mainly stearic acid,

48   SA) [11] which, in conjunction with activators ensure the formation of active Zn(II) centers [10].

49   More in depth, it is widely recognized that in the first reaction steps, ZnO interacts with SA to

50   create highly reactive Zn(II)-SA adducts, generally in the form of zinc stearate, which then react

51   with both accelerator and sulfur, providing Zn complexes containing poly-sulfidic ligands, which

52   represent the active sulfurating agents [10-12]. These units are believed to drive the subsequent

53   reactions with the polymer chains and the formation of poly-sulfidic pendant cross-link

54   intermediates, that progressively shorten through decomposition and rearrangement reactions

55   endorsed by Zn(II) sites, delivering highly cross-linked products [10-12].

56   Thus, the generation of zinc centers at the beginning of the reaction represents a critical step as it

57   determines both the reaction kinetic and the resulting properties of the cross-linked network [13].

58   In fact, several studies have demonstrated that the use of both ZnO and SA is crucial not only for

59   chemical cross-linking of the rubber molecules, but also for controlling structural polymer network

60   inhomogeneity in the sulfur cross-linked rubber [14-19]. Combining *in situ* time-resolved zinc K-

61   edge X-ray absorption fine structure spectroscopy, *in-situ* time-resolved Fourier-transform

62   infrared spectroscopy (FTIR), and density functional theory calculations, Ikeda and co-workers

63   proved the generation of a new dinuclear type bridging bidentate zinc/stearate complex composed

64   of $[Zn_2(\mu\text{-}O_2CC_{17}H_{35})_2]^{2+}\cdot4X$, where X is hydroxyl group, water and/or rubber segment [14-16].

65   This peculiar species was found to accelerate the hydrolysis reaction of CBS, the insertion reaction

66   of sulfur atoms along with the generation of abundant di-sulfidic linkages in the rubber compounds

67   [15].

68   In the last decade, we have pursued the study of the vulcanization process by exploring the

69   influence of Zn(II) centers dispersion and availability on the curing efficiency of isoprene rubber

70   (IR) [10, 20-22]. In detail, an innovative activator based on ZnO nanoparticles (NPs) directly

71   grown on the silica surface (ZnO/SiO_2), that behaves at the same time as a vulcanization activator

72   and a reinforcing filler, has been developed by exploiting soft-chemistry methods [20, 21].

73   Successively, the investigation has been also extended to Zn(II) single sites anchored on the

74   surface of SiO_2 NPs, through surface functionalization with amino silane followed by the

75   coordination of Zn(II) centers to the amino groups [22]. These materials having double

76   functionalities demonstrated higher efficiency in the curing process compared to microcrystalline

77   ZnO, conventionally employed as an activator for industrial rubber vulcanization, with a relevant

78   impact both on the reaction kinetics and on the dynamic mechanical properties of the vulcanized

79   composites, as well as reducing the whole amount of employed ZnO [20-22]. The results have

80   been ascribed to the unique characteristics of the activators, which supply Zn(II) catalytic sites

81   readily accessible to the curing agents, possibly endowing a reaction pathway where the formation

82   of the highly reactive zinc/stearate complexes retrieved by Ikeda et al. [14-16] boosts the curing

83   process.

84   Although the above-cited experimental evidences remarkably contributed to a better understanding

85   and control of the rubber vulcanization, it remains almost unexplored if and how the structural,

86 morphological and surface characteristics of the novel Zn-based activators effectively influence

87 their reactivity with SA, which represents a determinant step for the process efficiency. Try to face

88 with these challenges, the present investigation focuses on a comprehensive comparison between

89 the properties and the reactivity with SA of pure ZnO and ZnO/SiO_2 systems with different

90 structural, morphological and surface features. In a wider perspective, this study aims also at

91 unveiling how the anchoring of ZnO NPs with controlled morphological properties and its synergy

92 with SiO_2 support may influence the surface interaction with carboxylic species as SA.

93 Besides a careful characterization of the activators, an extensive spectroscopic survey carried out

94 by X-ray Photoelectron Spectroscopy (XPS) revealed the occurrence of various inequivalent zinc

95 and oxo-hydroxo species at the surface of ZnO NPs, possibly impacting on the Zn(II) reactivity

96 and complexation.

97 The interaction between the different ZnO/SiO_2 activators with SA, in the absence of rubber, was

98 studied by a combination of several techniques: Differential Scanning Calorimetry (DSC) and

99 ThermoGravimetric Analysis (TGA), to monitor and highlight different phase transitions, thermal

100 events and reaction products stability; FTIR and solid-state nuclear magnetic resonance (NMR)

101 spectroscopies to gain structural information on the SA coordination at the Zn sites. Through this

102 novel methodological approach, interesting correlations have been drawn among the

103 morphological and interfacial features of ZnO/SiO_2 systems, the thermal events observed in DSC

104 and the generation of different Zn(II)-SA complexes, as revealed by FTIR and NMR. Finally, in

105 order to demonstrate how these characteristics affect the vulcanization process, the proposed

106 ZnO/SiO_2 materials were tested as activators in the curing reaction of isoprene rubber (IR)

107 nanocomposites (NCs).

108 The results highlighted that morphology and surface control of the ZnO activators enable not only

109 a peculiar reactivity with stearic acid, but remarkably impact also on the vulcanization

110 performance delivered to the resulting rubber nanocomposites, providing specific hints for a better

111 design and implementation of efficient ZnO-based activators.

112

113 EXPERIMENTAL

114 *Materials.* Zinc acetate dihydrate ($\geq$ 98%), sodium hydroxide pellets (NaOH, $\geq$ 98%), ammonium

115 hydroxide solution (NH$_4$OH, 25%), tetraethylorthosilicate (TEOS) and SA (98%) were purchased

116 from Merck Life Science; absolute ethanol (EtOH) and water (for HPLC instrument) were

117 purchased from VWR International. For rubber NCs: cis-1,4-polyisoprene rubber (IR) was

118 purchased from Nizhnekamskneftechim Expor; bis(3-triethoxysilylpropyl) disulfide (TESPD)

119 from Aldrich; antioxidant N-(1,3-dimethylbutyl)-N'-phenyl-p-phenylenediamine (6PPD),

120 Santoflex-6PPD from Flexsys. The curing agents were purchased as follows: SA (Stearina TP8)

121 from Undesa; N-cyclohexyl-2-benzothiazole sulphenamide (CBS), Vulkacit CZ/X from Lanxess;

122 sulfur Creso from Redball Superfine; ZnO (wurtzite, specific sur-face area 5 m^{2}g^{-1}) from Zincol

123 Ossidi.

124 *Synthesis of ZnO/SiO$_2$.* ZnO/SiO$_2$ NPs were prepared by a two-step procedure, developed by

125 modifying an established previously reported approach [20]. The method is relatively fast, and it

126 generally enables the control of both ZnO NPs loading and distribution on the silica surface.

127 In the first step, SiO$_2$ particles with spherical shape, nanometric size (d = 60-70 $\pm$ 5 nm) and BET

128 specific surface area SSA$_{BET}$ = 66.6 $\pm$ 0.8 m^{2}g^{-1}, were prepared according to a conventional Stöber

129 method [23, 24]. ZnO NPs were then grown onto the silica surface exploiting the method reported

6

130   in [20]. Briefly, $Zn(CH_3COO)_2 \cdot 2H_2O$ (0.337 g) and NaOH (0.28 g) were dissolved in 70 mL of

131   EtOH or water at 65°C. Then, 1.0 g of SiO_2 NPs was then poured into the former zincate solution

132   and kept under stirring at 65 °C for 20 min, to promote the generation of ZnO NPs by hydrolysis

133   and condensation on the silica surface. The product was filtered, successively washed with EtOH

134   (or water, respectively) and dried in air at room temperature (RT). The nominal composition of

135   the catalyst corresponds to 12 wt. % of ZnO on SiO_2. The samples obtained from EtOH and H_2O

136   as solvents were labelled as ZnO/SiO_2_EtOH and $ZnO/SiO_2\_H_2O$, respectively. As reference

137   material, bare ZnO NPs were synthesized with the same protocol in water without silica addition

138   and labelled simply as ZnO.

139   ***Structural, morphological and surface characterization of ZnO/SiO₂ activators.*** The loading of

140   Zn in the samples was determined by Inductively Coupled Plasma Optical Emission Spectrometry

141   (ICP-OES), using a PerkinElmer OPTIMA7000 DV spectrophotometer. Specimens for the

142   analysis were prepared by dissolving 0.20 g of powdered samples in a Teflon beaker with 4.0 mL

143   of HNO_3, 3.0 mL of HCl and 1.0 mL of HF. The dispersion was diluted with 12 mL of milli-Q

144   H_2O and then further diluted to 1:100.

145   Powder X-ray diffraction (PXRD) patterns were collected with a Rigaku Miniflex 600

146   diffractometer (Cu Kα radiation) in the 2θ range 10-80° (2θ step 0.020°, 1 ° min^{-1} scan rate).

147   High-resolution transmission electron microscopy (HRTEM) was performed using a JEOL JEM-

148   2100 Plus apparatus operating at 200 kV and equipped with an 8-megapixel Gatan RioTM

149   complementary metal-oxide-semiconductor (CMOS) camera. A 5 µL drop of ethanol powder

150   samples suspension was deposited onto a carbon coated copper mesh grid for TEM investigation.

151 Reflectance UV–vis analysis (range 400–200 nm) was performed by a UV Lambda 900 Perkin

152 Elmer spectrometer on powdered samples to determine the absorption edge energy of ZnO. The

153 absorption onset can be obtained by plotting F(R) vs. energy according to the Kubelka Munk

154 equation [25] and the band gap energy (E_g) derived from the intercept point of the tangents to the

155 curve at the slope and at the minimum.

156 Structural information on ZnO/SiO_2 systems was achieved by solid state NMR. Experiments were

157 carried out with a Bruker 400WB spectrometer operating at a proton frequency of 400.13 MHz.

158 Magic Angle Spinning (MAS) NMR spectra were acquired with cross polarization (CP) sequence

159 under the following conditions: ^{29}Si frequency: 79.48MHz, contact time 5 ms, decoupling length

160 6.3 μs, recycle delay: 10 s, 5 k scans. Samples were packed in 4 mm zirconia rotors, which were

161 spun at 6.5 kHz under air flow. Q8M8 was used as external secondary reference. According to the

162 common ^{29}Si NMR notation, the Si species are labelled Q^n, where Q represents SiO_4 structural

163 units, and n is the number of bridging oxygens.

164 The surface chemical composition of the ZnO/SiO_2 powders was investigated by XPS. The

165 measurements were performed on the as-prepared powder samples, fixing them on the sample

166 holder using carbon tape. The XPS spectra were acquired in ultrahigh vacuo (base pressure: ~5 ×

167 10^{-10} mbar) at RT in normal emission geometry using a conventional Mg X-ray source (hν =

168 1253.6 eV) and a hemispherical electron energy analyzer (120 mm by PSP: total energy resolution

169 ~ 0.8 eV, standard deviation ± 0.2 eV). Due to charging effects, all binding energies (BE) were

170 calibrated by fixing the C 1s BE of atmospheric contamination at 284.8 eV. Survey scans were

171 obtained in the 0–1100 eV range, while detailed scans were recorded in the BE regions

172 corresponding to O 1s, C 1s, Si 2p, and Zn 2p levels. The O 1*s* and Zn 2*p3/2* XPS spectra were

173 reproduced by fitting the experimental data using a Shirley background and several Doniach-

174 Sunjich components, corresponding to different oxidation states and chemical environments.

175 ***Study of the SA interaction with ZnO/SiO_2 samples.*** The interaction of SA with ZnO/SiO_2

176 samples was investigated by DSC, which allows to monitor different phase transitions, thermal

177 events and to earn information about the possible generation/evolution of reaction products.

178 Components (SA and ZnO/SiO_2, 1:1 molar ratio) were mixed in a mortar to obtain a homogeneous

179 powder. Samples (5-8 mg) were weighted on a microbalance, compressed to ensure good thermal

180 contact, and enclosed in a 40 μL aluminum pan with pierced lid. To simulate the conditions of the

181 vulcanization reaction, mixtures were heated in a DSC-1 system (Mettler Toledo). Experiments

182 were performed using a three steps temperature ramp: i) temperature was increased starting from

183 30 to 200 °C with a heating rate of 5 °C min^{-1}; ii) samples were brought back to 30°C (heating rate

184 -10 °C min^{-1}); iii) a final heating step to 200 °C (heating rate 5 °C min^{-1}) was lastly performed. All

185 the experiments were carried out under nitrogen flow (80 mL min^{-1}).

186 The samples recovered from DSC and thus reacted with SA were analyzed by TGA to inspect the

187 thermal stability of the reaction products, also in comparison to that of pure SA and bare crystalline

188 zinc stearate. Experiments were performed using a TGA/DCS1 STARe SYSTEM in the

189 temperature range 30-700 °C, constant air flow (50 mL min^{-1}), heating rate of 10 °C min^{-1}; an

190 isothermal step at 200 °C (15 min) was used to complete the weight loss due to physisorbed solvent

191 molecules and water.

192 To gain structural information on the SA coordination at the Zn centers, ZnO/SiO_2_EtOH and

193 $ZnO/SiO_2\_H_2O$ powders after DSC were initially analyzed by FTIR in Attenuated Total

194 Reflectance mode (ATR-FTIR with a monolithic diamond crystal). Spectra were acquired using a

9

195 Perkin Elmer Spectrum 100 instrument in the region 650–4000 cm^{-1} and with a resolution of 2 cm^{-}

196 ^{1} (32 scans).

197 More detailed information on the local binding modes of carboxylic groups of SA at the interface

198 of ZnO/SiO$_2$ samples were achieved by ^{13}C solid state NMR experiments, which were recorded

199 with cross polarization pulse sequence at spinning rate of 6.5 kHz under the following conditions:

200 ^{13}C frequency 100.48 MHz, contact time 2 ms, decoupling length 5.9 µs, recycle delay: 3 s, 4k

201 scans. Adamantane was used as external secondary reference.

202 ***Preparation of silica/IR nanocomposites.*** The performance of ZnO/SiO$_2$ curing activators for the

203 vulcanization of rubber-based materials were preliminary tested by preparing silica/IR NCs. The

204 ingredients were mixed in a Brabender Plasti-Corder lab station internal mixer (65 mL mixing

205 chamber, 0.6 filling factor, 60 rpm rotor speed). First, IR was masticated into the mixing chamber

206 at 145 °C and a suitable amount of ZnO/SiO$_2$ and bare SiO$_2$ were added, in order to have 1.85 parts

207 per hundred (phr) of ZnO and 40 phr of SiO$_2$ filler, respectively, along with TESPD

208 compatibilizing agent (3.2 phr). After 3 min of mixing, the antioxidant 6-PPD (2.0 phr) and SA

209 (2.0 phr) were added and further mixed for 1 min. The composites were then reloaded into the

210 mixing chamber at T = 90 °C and CBS (3.0 phr) and S$_8$ (1.6 phr) were added (2 min of mixing).

211 Finally, the NCs were mixed in a two-rolling mill at 50 °C for 3 min, to improve their homogeneity.

212 Reference IR NCs were prepared by using bare SiO$_2$ filler (40 phr) and microcrystalline ZnO

213 curing activator (1.85 phr). The vulcanization reaction was performed by using a Rubber Process

214 Analyzer (RPA2000, Alpha Technologies). The vulcanization curves were registered at 170 °C

215 and 100 bar (frequency = 1.670 Hz, angle = 6.980 °) for a vulcanization time = 5 min, by measuring

216 the torque requested to keep the rotor at a constant rate over the time to evaluate the viscosity.

217   RESULTS AND DISCUSSION

218   **Structural and morphological characterization of ZnO/SiO₂ activators**.

219   The ZnO amount in the prepared activators was assessed by ICP-OES analysis and resulted 8.5±0.1

220   wt. % and 8.9±0.1 wt. % for ZnO/SiO$_2$_EtOH and ZnO/SiO$_2$_H$_2$O, respectively, i.e. values merely

221   similar to the nominal ones (~ 12 wt. %), with a reaction yield of about 70 % in both cases.
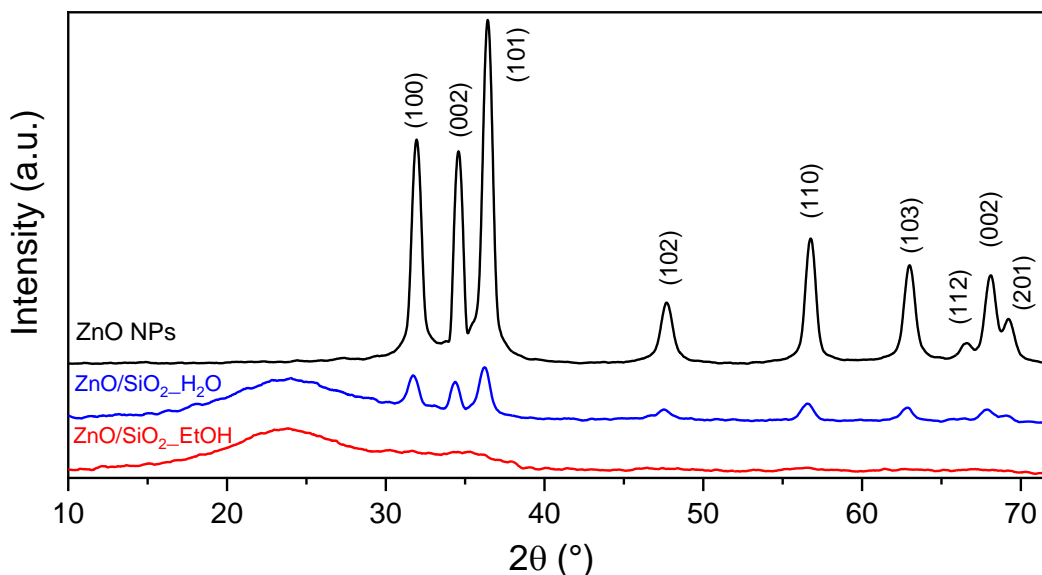
222   **Figure 1.** Powder XRD patterns of bare ZnO NPs (black line), ZnO/SiO$_2$_EtOH (red line) and

223   ZnO/SiO$_2$_H$_2$O (blue line) systems. All the indexed peaks are matched with the planes of the ZnO

224   hexagonal wurtzite structure (JCPDS no.36-1451).

225   The structural features of ZnO and ZnO/SiO$_2$ powders were investigated by PXRD (Figure 1).

226   Besides the broad band at ~ 22 ° connected to the presence of amorphous SiO$_2$ NPs, the typical

227   reflections of hexagonal wurtzite ZnO crystal phase (JCPDS no.36-1451) are clearly detectable

228   for ZnO and ZnO/SiO$_2$_H$_2$O NPs, while they appear just roughly sketched in the sample prepared

229   in EtOH. The sharp peaks observed for pure ZnO and, though less intense, in ZnO/SiO$_2$_H$_2$O

230   suggest a higher crystallization degree and an increased average size of the ZnO NPs compared to

231 the ZnO/SiO$_2$_EtOH system. Moreover, according to the Bragg's law, wurtzite peaks in bare ZnO

232 NPs lie at higher diffraction angles than ZnO/SiO$_2$_H$_2$O NPs, indicating a smaller lattice spacing

233 within the nanostructure, probably connected to the occurrence of oxygen vacant regions. Along

234 the same line, the shift of the reflections of ZnO/SiO$_2$_H$_2$O towards lower 2θ values envisages the

235 presence of zinc interstitial species in the oxide lattice, leading to larger interplanar distances.
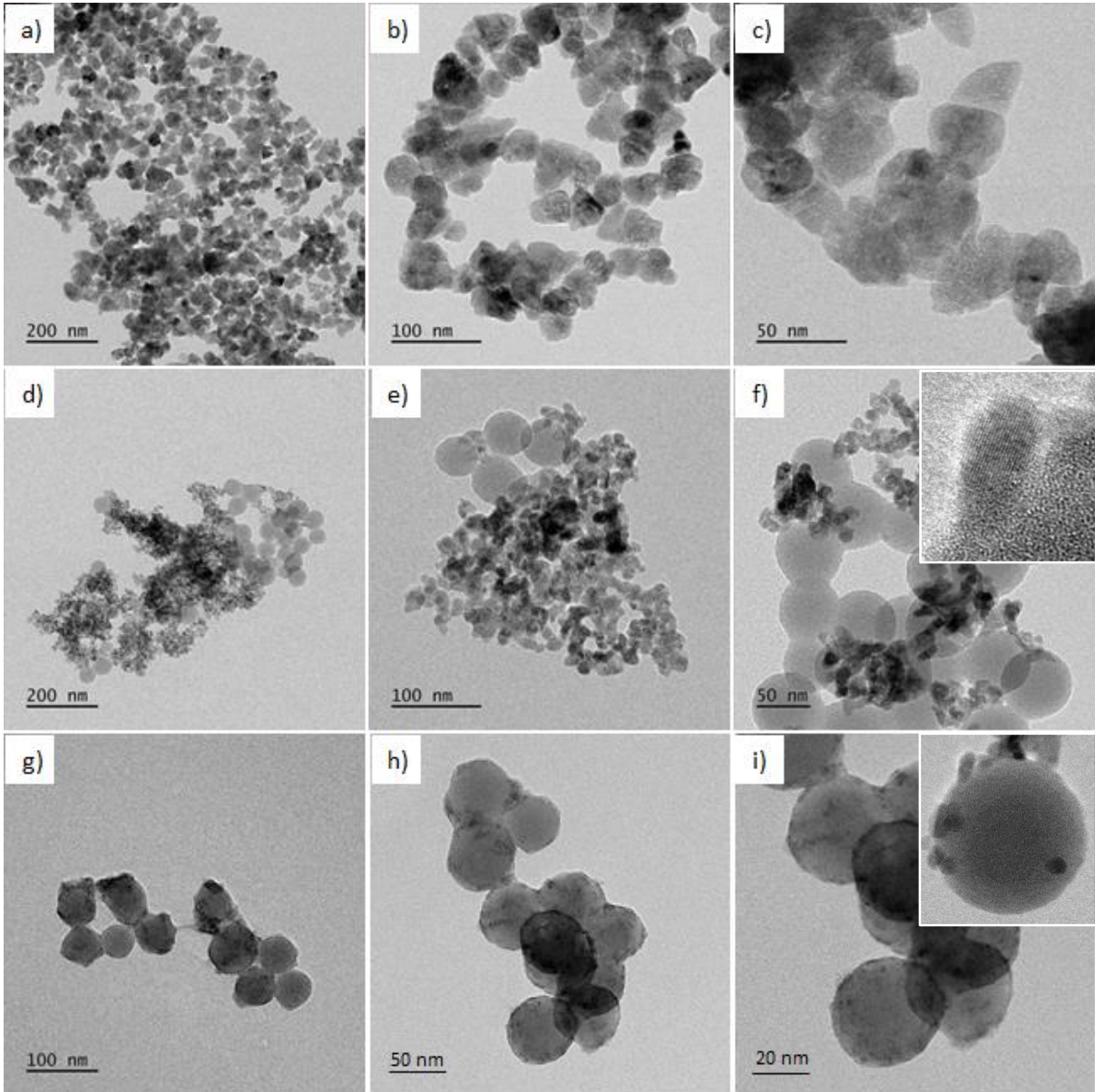
236 **Figure 2.** TEM images of: a)-c) bare ZnO NPs; d)-f) ZnO/SiO$_2$_H$_2$O and g)-i) ZnO/SiO$_2$_EtOH.

237 Inset in f) and i) highlights the ZnO NPs anchored on the surface of amorphous silica.

238 The morphological features of ZnO and ZnO/SiO$_2$ samples were investigated by TEM (Figure 2).

239 In detail, the images reveal that bare ZnO is constituted by micrometric or submicrometric

240 agglomerates of irregularly shaped NPs (Figure 2a) with average length of ~ 30-40 nm (Figure 2b,

241 c). In the case of ZnO/SiO$_2$_H$_2$O, separate aggregates can be observed (Figure 2d), where small

242 ZnO NPs (average diameter of ~ 10-15 nm) cover or bridges the larger silica nanospheres (Figure

243 2e,f). High resolution images (HRTEM, inset in Figure 2f) allow to identify crystallographic

244 planes in ZnO NPs, thus corroborating the crystallinity assessed by PXRD.

245 For ZnO/SiO$_2$_EtOH TEM images show silica nanospheres uniformly decorated by very tiny and

246 amorphous ZnO NPs (Figure 2g,h), whose occurrence can be revealed only at very large

247 magnifications (Figure 2i and inset). Also in this case, the results of TEM images are in agreement

248 with those retrieved by PXRD pattern.

249 UV-Vis spectroscopy was performed to further confirm the generation of ZnO NPs in ZnO/SiO$_2$

250 systems (Figure 3).
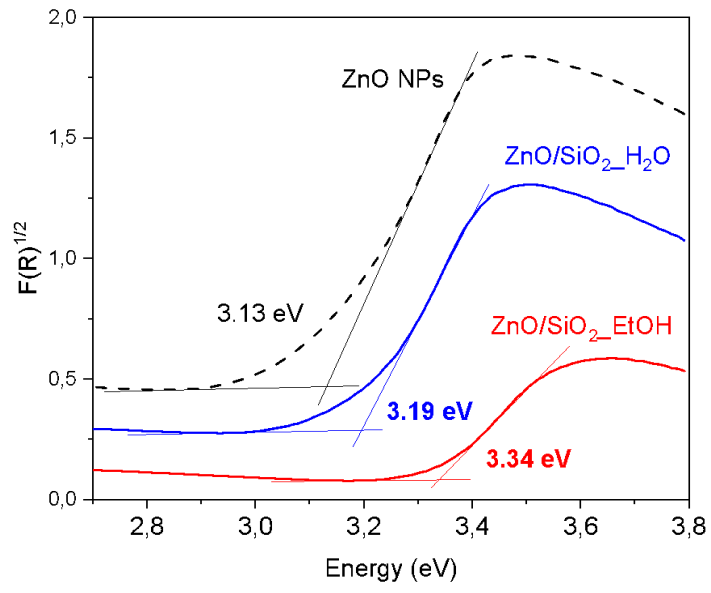
251

252 **Figure 3.** UV-Vis spectra of bare ZnO NPs (black-line), ZnO/SiO$_2$_EtOH (red-line) and

253 ZnO/SiO$_2$_H$_2$O (blue-line) systems elaborated according to the Kubelka Munk equation [25]. The

254 intercept between the tangents to the curve slope and the minimum value corresponds to the E$_g$

255 value.

256 For ZnO/SiO$_2$_H$_2$O sample, where the largest ZnO NPs are present, a band gap energy

257 (Eg = 3.19 eV) very similar to that of bulk ZnO is observed. Conversely, a progressive energy

258 blue-shift is detectable for ZnO/SiO$_2$_EtOH (Eg = 3.34 eV), corroborating the smaller ZnO NPs

259 dimensions revealed by TEM for this activator. These results are in agreement with our previous

260 investigation on mesoporous silica NPs decorated by ZnO [20, 21] and support the presence of the

261 oxide NPs in ZnO/SiO$_2$_EtOH.

262
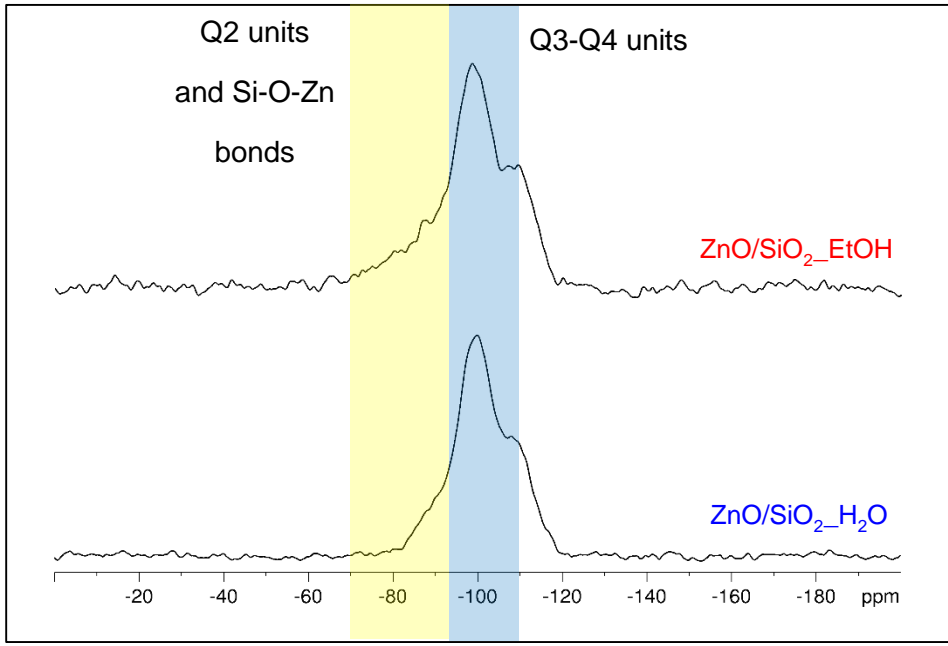
263 **Figure 4**. ^{29}Si CPMAS NMR spectra of ZnO/SiO$_2$_EtOH (above) and ZnO/SiO$_2$_H$_2$O (below).

264 In order to study the interaction between ZnO NPs and SiO$_2$ with a particular focus on the Si-O-

265 Zn bond formation, the ^{29}Si CPMAS spectra of the ZnO/SiO$_2$ systems are reported (Figure 4). Both

266 spectra are characterized by the Q signal that can be fitted with the silica Q^4 and Q^3 resonances

267 between -90 and -110 ppm, together with a superimposition of a broad shoulder in the range from

268 -70 to -90 ppm, which could account for both silica Q^2 resonance and signals due to Si units

269 substituted with a variable number of Si-O-Zn bonds [20].

270 An in depth semi-quantitative analysis of the CPMAS spectra has been performed in order to

271 inspect potential differences in the anchoring of ZnO at the silica surface. The results are

272 summarized in Table 1. As stated above, the Q resonance can be adequately fitted with 5

273 components centred at about -109, -100, -94, -88, -81 and -74 ppm. By comparison with the ^{29}Si

274 spectrum of the bare SiO_2 NP (not shown), the components at -109, -100 and -88 ppm are assigned

275 to Q^4, Q^3 and Q^2 silica units. Consequently, the other components represent the partial substitution

276 of Si-O-Si and Si-OH bonds with Si-O-Zn bonds on the particle surface (Q^nZn_m units, with m

277 number of Zn bonded to a SiO_4 unit), proving the effective anchoring of the ZnO NPs [21]. This

278 is indirectly confirmed by the reduction of surface Q^3 units compared to bare SiO_2 (see Table 1).

279 Moreover, the presence of additional Q_nZn_m components (at -74 and -81 ppm) in the

280 ZnO/SiO_2_EtOH spectrum indicates a more efficient anchoring compared to ZnO/SiO_2_H_2O.

281 **Table 1**. ^{29}Si CP-MAS NMR semi-quantitative results: relative amount and assignment of the main

282 identified units.

| Assign.		Q^nZn_m	Q^nZn_m	Q2/ Q^nZnm	Q^nZn_m	Q3	Q4
δ(iso)		*-74,3*	*-80,9*	*-87,9*	*-93,7*	*-99,7*	*-109,5*
SiO_2	%	--	--	12,7	--	67,6	19,7
ZnO/SiO_2_H_2O	%	--	--	7,8	11,9	50,4	29.9
ZnO/SiO_2_EtOH	%	3,6	3,7	10,9	9,4	45,7	26,8

283

284 It is worth to mention that Table 1 reports only an attempt of attribution. As a matter of facts, the

285 substitution, with consequent changes in the torsion angles T-Ô-T (T stands for a generic cation),

286 pushes downfield the related resonances with respect to the pure components [26], but both the

287 small shift and the intrinsic broadness of the components prevent the possibility of a definite

288 assignment of substituted Q^n unit.

289 These data drove to the conclusion that a different anchoring of the ZnO NPs on the silica surface

290 was obtained according to the synthetic conditions. The spectrum of ZnO/SiO$_2$_EtOH sample,

291 characterized by mainly small amorphous ZnO NPs, shows a wider left shoulder in the range -70

292 to -100 ppm, due to the higher presence of Si-O-Zn components, with respect to ZnO/SiO$_2$_H$_2$O

293 sample (decorated with both amorphous and crystalline ZnO NPs, that tend to aggregate). This

294 result suggests that both the NPs size and aggregation remarkably influence the growth and

295 distribution of ZnO on SiO$_2$ surface.

296 XPS analysis was carried out to further study the surface composition of the prepared ZnO/SiO$_2$

297 systems. The typical XPS wide survey spectra of ZnO/SiO$_2$ samples and of the reference pure ZnO

298 sample are showed in Figure S1 of the Supporting Information (SI), which reports the Zn, O and

299 C detected peaks. The presence of C in the samples may be ascribed both to residual acetate species

300 derived from the Zn precursor utilized for the materials synthesis and to the adventitious carbon

301 adsorbed on the surface during the exposure of the samples to the ambient atmosphere. The BE

302 values were corrected for the charge shift using as a reference the C 1s peak of graphitic carbon

303 (BE = 284.8 eV). Figure 5a displays the Zn $2p_{3/2}$ XPS spectra of ZnO, ZnO/SiO$_2$_EtOH and

304 ZnO/SiO$_2$_H$_2$O. While in pure ZnO, the Zn $2p_{3/2}$ level is detected at BE ~ 1021.7 ± 0.2 eV typical

305 of Zn−O ionic binding in agreement with the literature [27], for ZnO/SiO$_2$ activators is found at

306 slightly higher BE ~1022.1 ± 0.2 eV. This shift to higher BE suggests a change in the binding state

307 of Zn ions, which can be induced by the formation of Zn–O–Si bonds at the interface between the

308 ZnO and SiO_2 NPs in ZnO/SiO_2 samples and/or to non-linear charging effects often observed in

309 insulating samples [28] (not accounted by the alignment of the spectra at C 1s peak mentioned

310 above). Moreover, a contribution deriving from Zn species in ZnO(OH) or Zn(OH) environment

311 cannot be excluded, particularly for ZnO/SiO_2_EtOH system [21].

312 Spectra deconvolution (Figure 5a) enables to notice the presence of another component, located at

313 lower BE (~ 1020.0 ± 0.2 eV), which appears much more relevant in ZnO/SiO_2_H_2O. The overall

314 shift of Zn $2p_{3/2}$ core level to lower BE in ZnO-based materials usually reflects a change in the

315 binding state of Zn ions, which can be ascribed to a different coordination in the oxide lattice or to

316 a loss in the number of oxygen ions in nanocrystalline ZnO (i.e. oxygen defects) [29, 30]. However,

317 it has to be mentioned also that the presence of zinc interstitials species near the surface of ZnO

318 may contribute to the depletion of BE value [29].
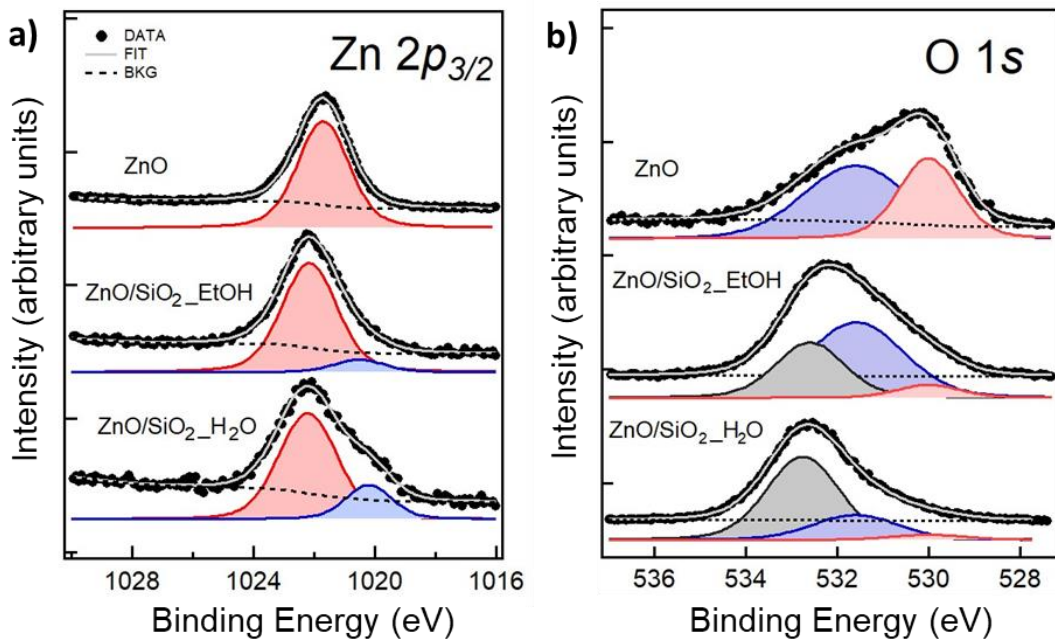
319

320 **Figure 5.** a) Zn $2p_{3/2}$ and b) O 1s XPS spectra of ZnO, ZnO/SiO_2_EtOH and ZnO/SiO_2_H_2O

321 samples.

17

322 O 1s XPS spectra of ZnO, ZnO/SiO$_2$_EtOH and ZnO/SiO$_2$_H$_2$O samples (Figure 5b) display

323 remarkable differences. The O 1s level in ZnO is significantly broad, suggesting the occurrence of

324 oxygen species in a different chemical environment. Indeed, spectral deconvolution results in

325 different bands centered at 530.0 ± 0.2 eV and 531.6 ± 0.2 eV (Figure 5b), which are assigned to

326 lattice oxygen (O$_{lattice}$) in the wurtzite structure and to ZnO(OH)/Zn(OH) species, respectively [31].

327 Besides the occurrence of O$_{lattice}$ and ZnO(OH)/Zn(OH), an additional peak at 533.0 ± 0.2 eV can

328 be revealed by fitting ZnO/SiO$_2$ spectra (Figure 5b), which is attributable to loosely bound oxygen

329 in the amorphous SiO$_2$ NPs or partially weakly adsorbed oxygen species such as water [32].

330 Accordingly, this latter contribution appears more evident in ZnO/SiO$_2$_H$_2$O than in

331 ZnO/SiO$_2$_EtOH NPs where, instead, the band related to ZnO(OH)/Zn(OH) species dominates the

332 spectrum (Figure 5b). In summary, the XPS survey thus unveils significant differences between

333 the surfaces properties of ZnO/SiO$_2$ systems, which may envisage a specific reactivity.

334

Study of the SA interaction with ZnO/SiO$_2$ samples

336 In the first step of the vulcanization mechanism ZnO interacts with SA leading to reactive Zn(II)-

337 SA adducts which, upon reaction with the accelerator and sulfur, provide Zn complexes bearing

338 polysulfidic ligands, behaving as the active sulfurating agents [1-11].

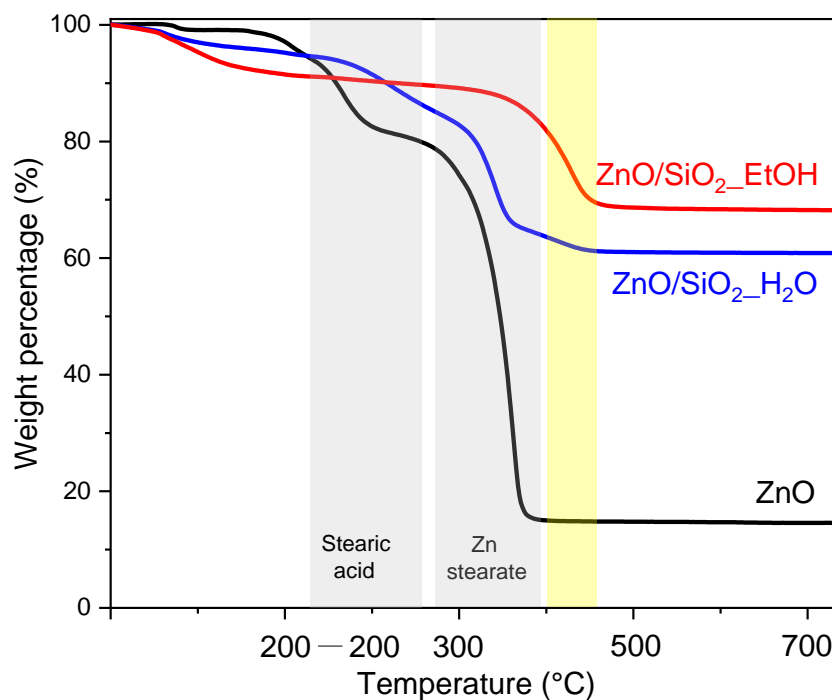339 In an attempt to mimic this initial passage, the interaction between SA and ZnO/SiO$_2$ systems was

340 explored through DSC. In detail, following the seminal works on the argument carried out by

341 Kruger and McGill [33-34], the measurements were performed in the solid-state by mixing the

342 samples with SA and then heating to the conventional temperature conditions experienced during

343 the vulcanization process. Results are summarized in Figure 6.

344

18
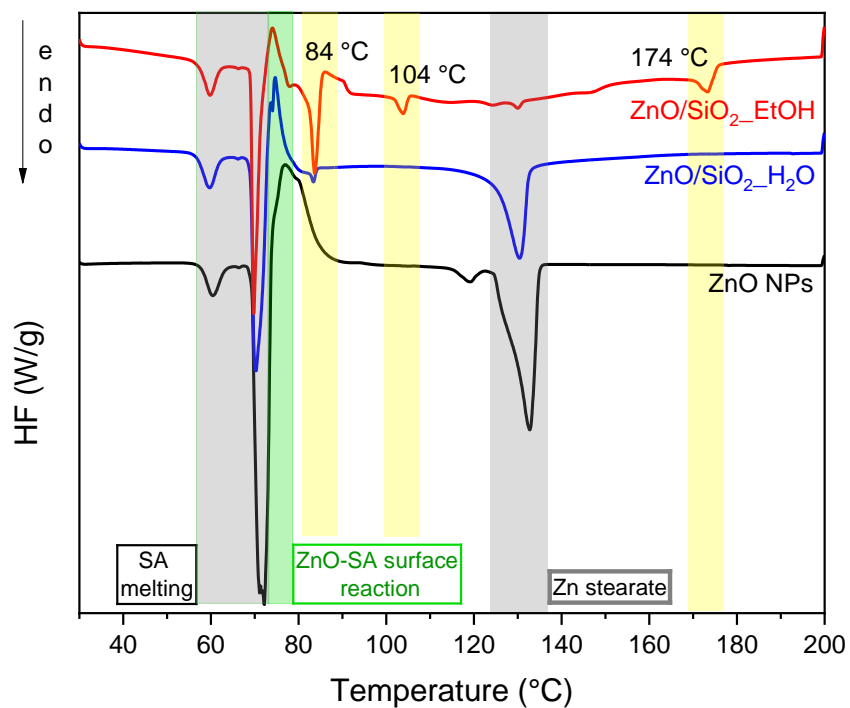
Figure 6. DSC curves of ZnO and ZnO/SiO$_2$ samples mixed with SA in the temperature range of 30-200°C.

During the first heating ramp, for both bare ZnO and ZnO/SiO$_2$ samples (Figure 6), an endothermic phenomenon in the temperature range 60-72 °C connected to the melting of free SA was observed [33], followed by an exothermic peak at ~ 80 °C. This was associated to the possible surface interaction between ZnO and SA, that occurs when the liquid SA gets closer to the surface of ZnO NPs. Besides, an additional endothermic peak at ~ 130 °C appears in all samples, probably associated to the melting of one of the reaction products, followed by its crystallization at ~ 115 °C during the cooling ramp (Figure S2a) and its further melting in the last heating ramp (Figure S2b). Interestingly, after the first heating ramp, ZnO/SiO$_2$ samples show the peak corresponding to that of the melting temperature typical of zinc stearate and no peaks due to SA, suggesting its total consumption. However, in the case of ZnO/SiO$_2$_EtOH, three new endothermic peaks are observed at 84, 104 and 174 °C, still present in the second heating ramp along with a small peak

19

359 due to zinc stearate. This suggests a peculiar reactivity of ZnO/SiO$_2$_EtOH with SA, which opens

360 the pathway to the formation of reaction products with distinctive structural properties, most likely

361 promoted by the diverse structural and surface properties of ZnO NPs.

362 Further insights on the products originated by ZnO-SA interaction were collected through TGA

363 analysis, which was performed after DSC treatment. In detail, TGA curve of ZnO NPs interacted

364 with SA reveals two main contributions to the weight loss (Figure 7, grey bands), ascribable to

365 residual SA (T_{onset} = 150 °C) and zinc stearate (T_{onset} = 260 °C), respectively.

366

367 **Figure 7.** Thermal degradation profiles of the reaction products formed after the interaction of

368 ZnO/SiO$_2$ samples with SA, compared to ZnO NPs interacted with SA. Grey bands evidence the

369 typical weight loss due to SA and Zn stearate. In yellow the presence of an additional component

370 with higher thermal stability is evidenced.

20

371 Reference thermal profiles of both SA and zinc stearate are reported in Figure S3. Similar

372 indications were obtained for ZnO/SiO$_2$_H$_2$O sample, where a small additional weight loss at T$_{onset}$

373 = 390 °C is detected too (Figure 7, yellow band). However, this latter contribution becomes

374 predominant in the case of ZnO/SiO$_2$_EtOH, where no weight losses due to SA and zinc stearate

375 were observed, thus confirming that the interaction of SA with ZnO/SiO$_2$_EtOH promotes the

376 generation of different reaction products characterized by a higher thermal stability than that of

377 zinc stearate.

378 The structural properties of the reaction products were preliminarily investigated by FTIR

379 spectroscopy (Figure 8). Spectrum of ZnO NPs interacted with SA (Figure 8, black line) exhibits

380 the main features of both SA and zinc stearate. In fact, the intense peak at 1750 cm^{-1} and the two

381 bands at 1538 cm^{-1} and 1398 cm^{-1} are assigned to the C=O stretching of COOH groups due to free

382 SA and to the asymmetric and symmetric stretching of COOH coordinated to zinc centers in the

383 structure of zinc stearate, respectively. This supports the formation of zinc stearate as the main

384 intermediate species generated in the first vulcanization steps, through the solubilization of Zn

385 centers of ZnO with SA. When ZnO/SiO$_2$ samples were reacted with SA, no residual SA was

386 detected at the end of the reaction, suggesting a possible higher reactivity of these systems

387 compared to bare ZnO. Indeed, signals ascribable to different reaction products appeared in the

388 spectra of both ZnO/SiO$_2$_H$_2$O and ZnO/SiO$_2$_EtOH (blue and red lines in Figure 8, respectively).

389 In particular, ZnO/SiO$_2$_H$_2$O reacted with SA shows: i) the typical signals at 1538 and 1398 cm^{-1}

390 assigned to the zinc stearate structure; ii) additional peaks at 1622, 1609 and 1595 cm^{-1}, along with

391 vibrations at 1420 and 1411 cm^{-1} possibly connected to surface zinc complexes with different

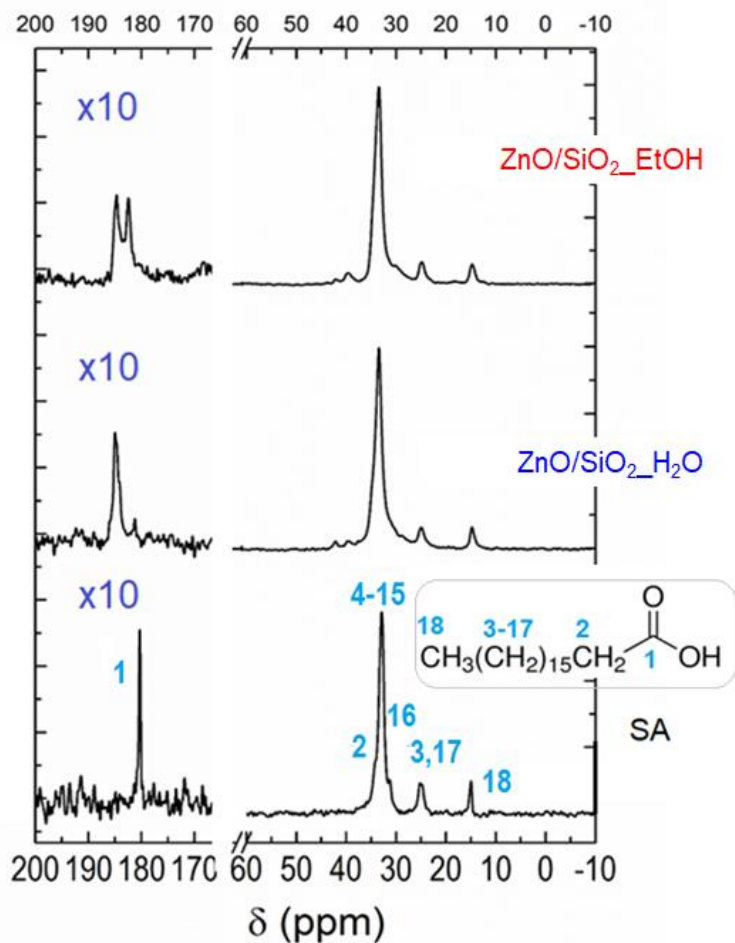392 structure. In the case of ZnO/SiO$_2$_EtOH, the peaks of zinc stearate were completely absent and

393   replaced by an intense band at 1560 cm^{-1}, adjacent to the very weak vibrations at 1622 and 1609

394   cm^{-1}, already observed in ZnO/SiO$_2$_H$_2$O.

395
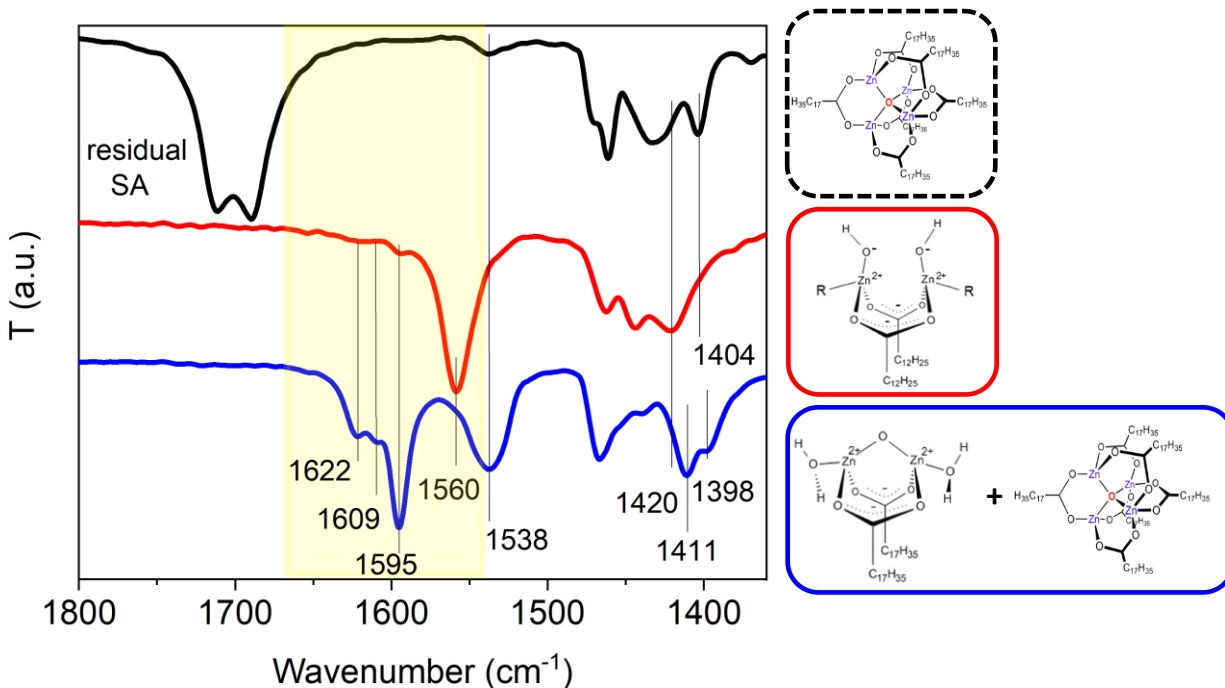
Figure 8. FTIR spectra of ZnO NPs (black line), ZnO/SiO$_2$_H$_2$O (blue line) and ZnO/SiO$_2$_EtOH

397   (red line) samples after the interaction with SA. The possible SA-ZnO structure are illustrated for

398   each sample on the side of the spectrum.

399   According to Ikeda et al. [14], the spectral features of ZnO/SiO$_2$ NPs indicate the presence of

400   dinuclear bridging bidentate coordinated zinc/stearate complexes, where each SA molecule

401   connects two zinc centers with a Zn:SA molar ratio equal to 1:1, leaving two free positions on each

402   Zn(II) sites for further ligands. In detail, for ZnO/SiO$_2$_H$_2$O, the vibrations resemble those

403   attributed to a skeleton composed of $[Zn_2(\mu-O_2CC_{17}H_{35})_2]^{2+}\cdot 4X$, where X is hydroxyl group, water

404   and/or acetate ligands (see Inset in Figure 8, red square). Instead, the further shift of the COO$^-$

405   stretching towards lower wavenumber observed for ZnO/SiO$_2$_EtOH, may be justified considering

22

406   the formation of a bridged oxo group between two zinc atoms instead of two hydroxyl groups

407   and/or acetate ligands (Inset in Figure 8, blue square). In addition, the peak at 1622 cm^{-1} detected

408   in both SiO_2/ZnO samples can be identified with non-bridged monodentate structures [35].

409   These results, besides matching with several previous studies [14-15, 20-21], endorse the

410   generation of different reaction products due to the SA interaction with ZnO/SiO_2 activators, in

411   line with DSC and TGA data.

412   The SA reactivity with ZnO/SiO_2 systems was further deepen by investigating the local binding

413   modes of the carboxylic acid at the oxide interface through ^{13}C solid state NMR. The spectra of

414   both ZnO/SiO_2 samples treated with SA and the pure SA are reported in Figure 9.

415   All the resonances belonging to SA are clearly detectable in the samples, with a slightly broader

416   shape than for the pure acid, due to a reduced mobility typical of the grafting process [36]. Most

417   interestingly, the carbonyl resonance (**1**) of SA at 180 ppm is both downfield shifted and split to

418   185 and 183 ppm in ZnO/SiO_2 systems. As this resonance represents a spectroscopic signature of

419   the binding mode of the carboxylic group to the metal oxide surface [36], the formation of the zinc

420   stearate complexes after ZnO-SA interaction was further confirmed. Moreover, the presence of

421   two signals indicates two possible geometries for the coordination of the fatty acid to the metal

422   centre [36-40] but the assignment to specific binding modes is not trivial.

423   As a matter of fact, according to the literature, the peak at 185 ppm could correspond to chelating

424   carboxylate carbons, whereas the 183 ppm signal could be assigned to dinuclear bidentate bridging

425   carboxylate carbons [36-40] or, in better agreement with IR results, they both could refer to

426   bidentate bridging $[Zn_2(\mu-O_2CC_{17}H_{35})_2]^{2+}\cdot4X$ with different X ligands. From a closer inspection,

427   these two resonances are present in the two samples with different ratios, equal to 51:40 and 96:4,

428   for ZnO/SiO_2_EtOH and ZnO/SiO_2_H_2O respectively. The different coordination mode is

23

429   reflected by the downfield shifted and doubled resonance of the α-CH$_2$ groups (**2**), which moves

430   from 34.3 ppm in SA to 39.7 and 42.1 ppm in both ZnO/SiO$_2$ samples [36]. The similarity of all

431   the other resonance indicates that the chain packing does not change among the samples.

432

Figure 9. ^{13}C CPMAS NMR spectra of the ZnO/SiO$_2$ samples after SA interaction, compared with

434   pure SA.

435   The above outcomes enable us to complete the picture drawn by DSC, TGA and FTIR analyses,

436   highlighting the occurrence of a peculiar reactivity for ZnO/SiO$_2$ systems with SA, evidently

437   connected to their structural, morphological and surface characteristics.

24

438 In particular, ZnO/SiO$_2$_EtOH NPs with poor crystallinity, tiny particle size and remarkable

439 presence of ZnO(OH)/Zn(OH) at the surface seems to promote the generation of ZnO-SA bridging

440 bidentate structures with high thermal stability. Conversely, the higher crystallinity, larger particle

441 size and lattice defectivity of ZnO/SiO$_2$_H$_2$O NPs drive the reaction with SA towards the

442 formation of a mixture of Ikeda-like complexes [14, 15] and other Zn stearate structures, with a

443 generally lower thermal stability.

444 These considerations are in agreement with both theoretical and experimental studies reported in

445 the literature, where carboxylate species on ZnO surfaces are found mostly adopting the most

446 thermodynamically favored bidentate configuration, whereas other adsorption configurations are

447 recognized only in the presence of defective sites (e.g. oxygen vacancies), like those detected by

448 XPS in ZnO/SiO$_2$_H$_2$O NPs. Moreover, previous reports on similar oxide systems describe a

449 correlation between the occurrence of OH groups at the ZnO surface and the bridging bidentate

450 configuration obtained upon interaction of SA with ZnO/SiO$_2$_EtOH.

451 The generation and the chemical structure of these specific Zn(II)-SA vulcanization intermediates

452 was finally related to the peculiar behavior imparted by ZnO/SiO$_2$_EtOH and ZnO/SiO$_2$_H$_2$O

453 activators to the curing of silica/isoprene NCs, as reported in Figure 10. In detail, the vulcanization

454 curves were registered by measuring the torque (S') values over the curing time and the

455 performance were compared to that of conventionally IR NCs prepared using microcrystalline

456 ZnO. The sulfur cross-link formation between polymer chains is responsible for the higher

457 viscosity of the vulcanized materials and is connected to the measured S' increase.

458

459

460

25
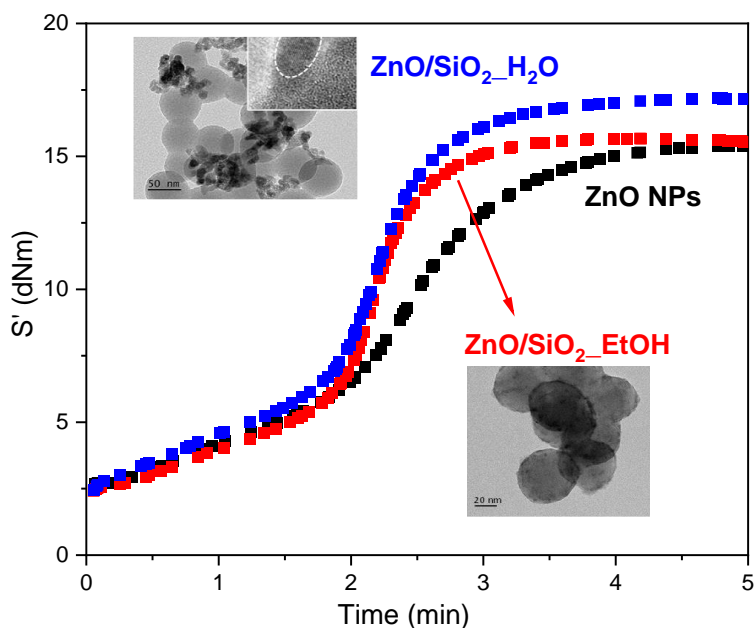
Figure 10. Vulcanization curves measured for silica/IR NCs vulcanized with ZnO/SiO_2_EtOH and $ZnO/SiO_2\_H_2O$ activators, compared to bare ZnO.

Comparing the curves, both ZnO/SiO_2 materials show higher maximum torque (M_{max}) and are characterized by a lower curing time (t_{90}, the time required for reaching 90% of M_{max} at the curing temperature) compared to pure ZnO. Moreover, an appreciable difference between the M_{max} values of ZnO/SiO_2_EtOH and $ZnO/SiO_2\_H_2O$ can be observed (Fig. 10), suggesting a distinct ability of the Zn(II)-SA complexes in supplying Zn(II) centers readily interacting with the other curing agents. However, clarifying the reason behind this difference is notoriously difficult, since it entails several other parameters influencing the vulcanization process, and it is currently part of an ongoing investigation.

Nevertheless, the overall results point out that morphology and surface control of the ZnO activators enable not only a peculiar reactivity with stearic acid, but remarkably impact also on the vulcanization performance delivered to the resulting rubber nanocomposites.

CONCLUSION

475

476 In this manuscript, we have studied the influence of the structural, morphological and surface

477 features of different ZnO/SiO_2 activators on their reactivity with SA, trying to gain valuable

478 information connected to the first step of the vulcanization mechanism.

479 Pursuing this target, a comprehensive characterization was initially performed through XRD and

480 TEM, which evidenced an effect of reaction solvent, EtOH or water, in providing amorphous and

481 tiny particles decorating SiO_2 nanospheres or crystalline and large ZnO nanocrystals bridging the

482 silica aggregates, respectively.

483 ^{29}Si solid state NMR and, more in depth, XPS investigation corroborated a distinct anchoring of

484 ZnO on the silica surface of ZnO/SiO_2 systems, unveiling the occurrence of inequivalent surface

485 properties: $ZnO(OH)/Zn(OH)$ species dominating in ZnO/SiO_2_EtOH NPs while oxygen defects

486 in $ZnO/SiO_2\_H_2O$ NPs. These characteristics lead to significant fallouts in the reactivity with SA,

487 which was performed and monitored by DSC. Different thermal events have been retrieved, which,

488 according to FTIR, TGA and ^{13}C NMR correspond to unique reaction products both in terms of

489 chemical architecture and of thermal stability. In detail, while for pure ZnO only zinc stearate

490 represents the exclusive detected species, unequal ZnO-SA bridging bidentate complexes, very

491 similar to those proposed by Ikeda and co-workers and described as determinant for the

492 vulcanization process, have been observed for SiO_2/ZnO NPs.

493 The chemical structure of these specific Zn(II)-SA vulcanization intermediates was finally proved

494 to be involved in the peculiar curing behavior imparted by ZnO/SiO_2_EtOH and $ZnO/SiO_2\_H_2O$

495 activators to silica/isoprene NCs.

496 The overall results suggest that careful tailoring of the features of ZnO activators offers the chance

497 to orient the initial step of the vulcanization mechanism toward the generation of specific

27

498 Zn(II)-SA intermediates, which significantly boost the yield of the curing process, with potential

499 economic and environmental benefits.

500 Finally, the methodological protocol adopted in this study may help to critically complement the

501 outstanding results already reported in the literature, by proposing a valid benchmark for achieving

502 further insights on the interaction of SA with activators, and in turn, with the other species involved

503 in the vulcanization mechanism.

504

505 ASSOCIATED CONTENT

506 **Supporting Information**. XPS wide survey spectra of ZnO and ZnO/SiO_2 samples; DSC curves

507 registered during the cooling ramp (200-30 °C) and the second heating ramp (30-200 °C); Thermal

508 profiles of zinc stearate and SA.

509 AUTHOR INFORMATION

510 **Corresponding Author**

511 * Prof. Massimiliano D'Arienzo, email: massimiliano.darienzo@unimib.it, phone number: 0039-

512 026448-5023

513 **Author Contributions**

514 The manuscript was written through contributions of all authors. All authors have given approval

515 to the final version of the manuscript.

522 ABBREVIATIONS

523 SA stearic acid; NPs nanoparticles; TEM Transmission Electron Microscopy; DSC Differential

524 Scanning Calorimetry; FTIR Fourier Transform Infrared Spectroscopy; NMR Nuclear Magnetic

525 Resonance; XPS X-ray Photoelectron Spectroscopy.

526 REFERENCES

527 [1] C.M. Blow, C. Hepburn, *Rubber Technology and Manufacture*, Butterworth Scientific, London

528 (1981), 2nd Ed.

529 [2] W. Hofmann, *Rubber Technology Handbook*, Hanser Publishers, New York (1994).

530 [3] M. Coleman, J. R. Shelton, J. L. Koenig. Sulfur Vulcanization of Hydrocarbon Diene

531 Elastomers. *Ind. Eng. Chem. Prod. Res. Dev.* 13 (1974) pp 154 –166

532 [4] M. R. Krejsa, J. L. Koenig. A Review of Sulfur Crosslinking Fundamentals for Accelerated

533 and Unaccelerated Vulcanization. *Rubber Chem. Technol.* 66 (1993) pp 376 – 410

534 [5] F. Ignatz-Hoover. Review of Vulcanization Chemistry. *Rubber World* 220 (1999) pp 24

535 [6] P. J. Nieuwenhuizen. Zinc Accelerator Complexes. Versatile Homogeneous Catalysts in

536 Sulphur Vulcanization. *Appl. Catal. A Gen.* 207 (2001) pp 55 – 68

537 [7] G. Heideman, R. N. Datta, J. W. M. Noordermeer, B. Van Baarle. Activators in Accelerated

538 Sulphur Vulcanization. *Rubber Chem. Technol.* 77 (2004) pp 512 – 541

539 [8] G. Heideman, R. N. Datta, J. W. M. Noordermeer, B. Van Baarle. Influence of Zinc Oxide

540 during Different Stages of Sulphur Vulcanization Elucidated by Model Compound Studies. *J.*

541 *Appl. Polym. Sci.* 95 (2005) pp 1388 – 1404

542 [9] Y. Ikeda, A. Kato, S. Kohjiya, Y. Nakajima. *Rubber Science: A Modern Approach*, Springer, Singapore (2017)

544 [10] S. Mostoni, P. Milana, B. Di Credico, M. D'Arienzo, R. Scotti. Zinc-Based Curing Activators: New Trends for Reducing Zinc Content in Rubber Vulcanization Process. *Catalysts* 9 (2019) pp 664

547 [11] G. Heideman. Reduced Zinc Oxide Levels in Sulphur Vulcanisation of Rubber Compounds. *Ph.D. Thesis*, University of Twente, Enschede, The Netherlands (2004)

549 [12] Coran, A. Y. 7 - Vulcanization. In *Science and Technology of Rubber* (Second ed.); Mark, J. E.; Erman, B.; Eirich, F. R., Eds.; Academic Press: San Diego, 1994; pp 339 – 385.

551 [13] P. Ghosh, S. R. Katare, P. R. Patkar, J. M. Caruthers, V. Venkatasubramanian, K. A. Walker. Sulfur Vulcanization of Natural Rubber for Benzothiazole Accelerated Formulations: From reaction mechanisms to a rational kinetic model. *Rubber Chem. Technol.* 76 (2003) pp 592 – 693

554 [14] Y. Ikeda, Y. Yasuda, T. Ohashi, H. Yokohama, S. Minoda, H. Kobayashi, T. Honma. Dinuclear Bridging Bidentate Zinc/Stearate Complex in Sulfur Cross-Linking of Rubber. *Macromolecules* 48 (2015) pp 462 – 475

557 [15] Y. Ikeda, Y. Sakaki, Y. Yasuda, P. Junkong, T. Ohashi, K. Miyaji, H. Kobayashi. Roles of Dinuclear Bridging Bidentate Zinc/Stearate Complexes in Sulfur Cross-Linking of Isoprene Rubber. *Organometallics* 38 (2019) pp 2363 – 2380

560 [16] Y. Ikeda, N. Higashitani, K. Hijikata, Y. Kokubo, Y. Morita, M. Shibayama, N. Osaka, T. Suzuki, H. Endo, S. Kohjiya. Vulcanization: New Focus on a Traditional Technology by Small-Angle Neutron Scattering. *Macromolecules* 42 (2009) pp 2741 – 2748

563   [17] Y. Yasuda, S. Minoda, T. Ohashi, H. Yokohama, Y. Ikeda. Two-Phase Network Formation

564   in Sulfur Crosslinking Reaction of Isoprene Rubber. *Macromol. Chem. Phys.* 215 (2014) pp 971

565   − 977

566   [18] P. Junkong, R. Morimoto, K. Miyaji, A. Tohsan, Y. Sakaki, Y. Ikeda. Effect of fatty acids on

567   the accelerated sulfur vulcanization of rubber by active zinc/carboxylate complexes. *RSC Adv.* 10

568   (2020) pp 4772 − 4785

569   [19] M. Hernández, T. A. Ezquerra, R. Verdejo, M. A. López-Manchado. Role of Vulcanizing

570   Additives on the Segmental Dynamics of Natural Rubber. *Macromolecules* 45 (2012) pp 1070–

571   1075

572   [20] A. Susanna, L. Armelao, E. Callone, S. Dirè, M. D'Arienzo, B. Di Credico, L. Giannini,

573   T. Hanel, F. Morazzoni, R. Scotti. ZnO Nanoparticles Anchored to Silica Filler. A Curing

574   Accelerator for Isoprene Rubber Composites. *Chem. Eng. J.* 275 (2015) pp 245 − 252

575   [21] A. Susanna, M. D'Arienzo, B. Di Credico, L. Giannini, T. Hanel, R. Grandori, F. Morazzoni,

576   S. Mostoni, C. Santambrogio, R. Scotti. Catalytic Effect of ZnO Anchored Silica Nanoparticles on

577   Rubber Vulcanization and Cross-Link Formation. *Eur. Polym. J.* 93 (2017) pp 63 − 74

578   [22] S. Mostoni, M. D'Arienzo, B. Di Credico, L. Armelao, M. Rancan, S. Dirè, E. Callone, R.

579   Donetti, A. Susanna, R. Scotti. Design of a Zn Single-Site Curing Activator for a More Sustainable

580   Sulfur Cross-Link Formation in Rubber. *Industrial & Engineering Chemistry Research* 60 (2021)

581   pp 10180 − 1019

582   [23] T. Wu, Y. Zhang, X. Wang, S. Liu. Fabrication of Hybrid Silica Nanoparticles Densely

583   Grafted with Thermoresponsive Poly(N-isopropylacrylamide) Brushes of Controlled Thickness

584   via Surface-Initiated Atom Transfer Radical Polymerization. *Chem. Mater.* 20 (2008) pp 101 −

585   109

586 [24] W. Stöber, A. Fink, E. Bohn. Controlled growth of monodisperse silica spheres in the micron

587 size range. *J. Colloid Interface Sci.* 26 (1068) pp 62 – 69

588 [25] S. Monticone, R. Tufeu, A. V. Kanaev. Complex nature of the UV and visible fluorescence

589 of colloidal ZnO nanoparticles. *J. Phys. Chem. B* 102 (1998) pp 2854 – 2862

590 [26] C. Bertail, S. Maron, V. Buissette, T. Le Mercier, T. Gacoin, J. P. Boilot. Structural and

591 Photoluminescent Properties of Zn2SiO4:Mn2+ Nanoparticles Prepared by a Protected Annealing

592 Process *Chem. Mater.* 23 (2011) pp 2961 – 2967

593 [27] M. A. Mahjoub, G. Monier, C. Robert-Goumet, F. Réveret, M. Echabaane, D. Chaudanson,

594 M. Petit, L. Bideux, B. Gruzza. Synthesis and study of stable and size-controlled ZnO–

595 SiO$_2$ quantum dots: application as a humidity sensor. *J. Phys. Chem. C* 120 (2016) pp

596 11652– 11662

597 [28] J. F. Moulder, W. F. Stickle, P. E. Sobol, K. D. Bomben. In *Handbook of X-ray Photoelectron*

598 *Spectroscopy*; Chastain, G., Ed.; Perkin Elmer Corporation: Eden Prairie (Minnesota), 1992.

599 [29] Y. Y. Tay, S. Li. Size dependence of Zn 2*p* 3/2 binding energy in nanocrystalline ZnO. *Appl.*

600 *Phys. Lett.* 88 (2006) pp 173118

601 [30] F. M. Chang, S. Brahma, J. H. Huang, Z. Z. Wu, K. Y. Lo. Strong correlation between optical

602 properties and mechanism in deficiency of normalized self-assembly ZnO nanorods. *Sci Rep* 9

603 (2019) pp 905

604 [31] L. L. Yang, Q. X. Zhao, M. Willander, X. J. Liu, M. Fahlman, J. H. Yang. Origin of the

605 surface recombination centers in ZnO nanorods arrays by X-ray photoelectron spectroscopy.

606 *Applied Surface Science* 256 (2010) pp 3592 – 3597

607 [32] Y. Y. Peng, T. E. Hsieh, C. H. Hsu. White-light emitting ZnO–SiO$_2$ nanocomposite thin films

608 prepared by the target-attached sputtering method. *Nanotechnology* 17 (2006) pp 174 – 180

609   [33] F. W. H. Kruger, W. J. McGill. A DSC study of curative interactions. I. The interaction of

610   ZnO, sulfur, and stearic acid. *J. Appl. Polym. Sci.* 42 (1991) pp 2643 – 2649,

611   [34] F. W. H. Kruger, W. J. McGill. A DSC study of curative interactions. II. The interaction of

612   2,2′-dibenzothiazole with ZnO, sulfur, and stearic acid. *J. Appl. Polym. Sci.* 42 (1991) pp 2651 –

613   2659

614   [35] M. A. Mesubi. An infrared study of zinc, cadmium, and lead salts of some fatty acids. *J. Mol.*

615   *Struct.* 81 (1982) pp 61 – 71

616   [36] J. Špačková, C. Fabra, S. Mittelette, E. Gaillard, C.-H. Chen, G. Cazals, A. Lebrun, S. Sene,

617   D. Berthomieu, K. Chen. Unveiling the Structure and Reactivity of Fatty-Acid Based

618   (Nano)Materials Thanks to Efficient and Scalable ^{17}O and ^{18}O-Isotopic Labeling Schemes. *J. Am.*

619   *Chem. Soc.* 142 (2020) pp 21068 – 21081

620   [37] J. De Roo, E. A. Baquero, Y. Coppel, K. De Keukeleere, I. Van Driessche, C. Nayral, Z.

621   Hens, F. Delpech. Insights into the Ligand Shell, Coordination Mode, and Reactivity of Carboxylic

622   Acid Capped Metal Oxide Nanocrystals. *ChemPlusChem* 81 (2016) pp 1216 – 1223

623   [38] B. H. Ye, X. Y. Li, I. D. Williams, X. M. Chen. Synthesis and structural characterization of

624   di- and tetranuclear zinc complexes with phenolate and carboxylate bridges. Correlations between

625   13C NMR chemical shifts and carboxylate binding modes. *Inorganic Chemistry* 41 (2002) pp 6426

626   –6431

627   [39] J. Catalano; Y. Yao, A. Murphy, N. Zumbulyadis, S. A. Centeno, C. Dybowski. Nuclear

628   Magnetic Resonance Spectra and 207Pb Chemical-Shift Tensors of Lead Carboxylates Relevant

629   to Soap Formation in Oil Paintings. *Appl. Spectrosc*. 68 (2014) pp 280 – 286

630   [40] A. Patra, T. K. Sen, R. Bhattacharyya, S. K. Mandal, M. Bera. Diversity of carboxylate

631   binding in a new tetranuclear zinc cluster: correlation between spectroscopic investigations and

632   carboxylate binding modes. *RSC Adv.* 2 (2012) pp 1774 – 1777

633

Studying stearic acid interaction with ZnO/SiO$_2$ nanoparticles with tailored morphology and surface features: a benchmark for better designing efficient ZnO-based curing activators

Silvia Mostoni [a], Paola Milana [a], Massimiliano D'Arienzo [a*], Sandra Dirè [b], Emanuela Callone [b], Cinzia Cepek [c], Silvia Rubini [c], Aysha Farooq [c], Carmen Canevali [a], Barbara Di Credico [a] and Roberto Scotti [a]

[a] Department of Materials Science, INSTM, University of Milano-Bicocca, Via R. Cozzi 55, 20125 Milano, Italy;

[b] Department of Industrial Engineering (DII), University of Trento, Via Sommarive 9, 38123, Trento, Italy;

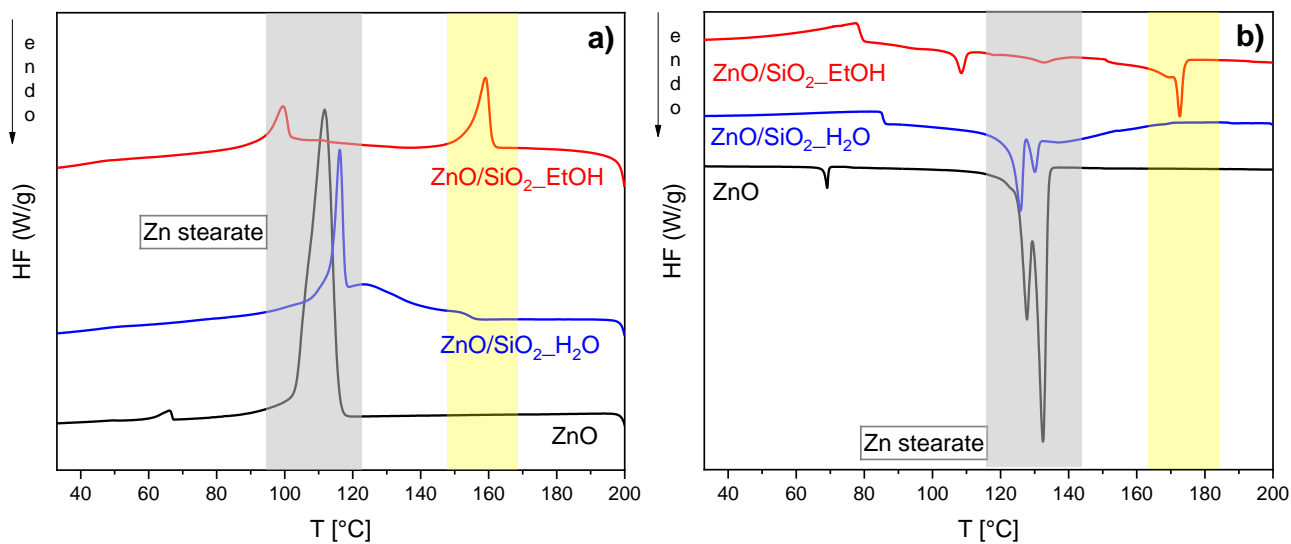[c] Istituto Officina dei Materiali-CNR Laboratorio TASC, Strada Statale 14, km 163.4, I-34012 Trieste, Italy

649

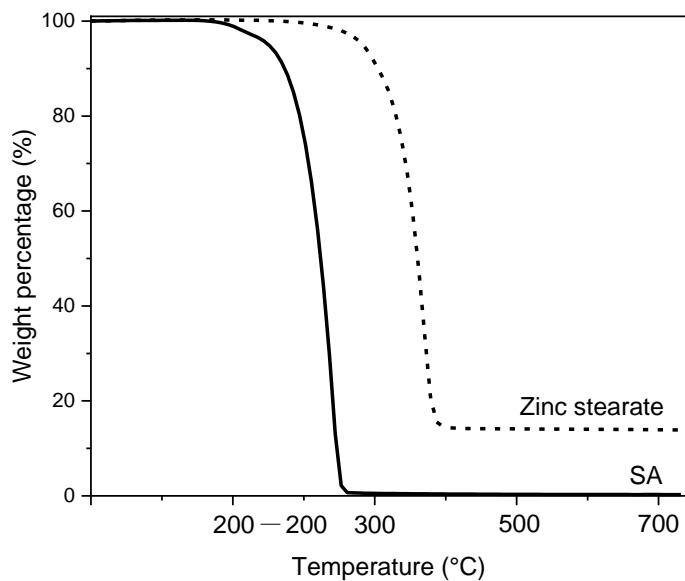**Figure S1.** XPS wide survey spectra of pure ZnO (black line), ZnO/SiO$_2$_EtOH (red line) and
ZnO/SiO$_2$_H$_2$O NPs (green line).

652

653

Figure S2. DSC curves of ZnO and ZnO/SiO$_2$ samples mixed with SA registered a) during the
cooling ramp (monitored from 200 to 30 °C) and b) during the second heating ramp (from 30 to
200°C).

657

Figure S3. Thermal degradation profiles of zinc stearate (dashed line) and SA (bold line).

658

659

660

661